PAPER • **OPEN ACCESS**

Drug-Loaded IRONSperm clusters: modeling, wireless actuation, and ultrasound imaging

To cite this article: Kaz I N A Middelhoek *et al* 2022 *Biomed. Mater.* **17** 065001

IOP Publishing Biomed. Mater. 17 (2022) 065001 https://doi.org/10.1088/1748-605X/ac8b4b

Biomedical Materials

OPEN ACCESS

RECEIVED
25 March 2022

REVISED
21 July 2022

ACCEPTED FOR PUBLICATION
19 August 2022

PUBLISHED
2 September 2022

PAPER

Drug-Loaded IRONSperm clusters: modeling, wireless actuation, and ultrasound imaging

Kaz I N A Middelhoek[1], Veronika Magdanz[2], Leon Abelmann[3,4] and Islam S M Khalil[1,*]

[1] Department of Biomechanical Engineering, University of Twente, Enschede, The Netherlands
[2] Institute for Bioengineering of Catalonia, Barcelona Institute of Science and Technology, Barcelona, Spain
[3] MESA+ Research Institute, University of Twente, Enschede, The Netherlands
[4] KIST Europe, Saarbrücken, Germany
[*] Author to whom any correspondence should be addressed.

E-mail: i.s.m.khalil@utwente.nl

Keywords: microrobot aggregation, sperm, drug delivery, magnetic actuation, ultrasound

Supplementary material for this article is available online

Abstract

Individual biohybrid microrobots have the potential to perform biomedical *in vivo* tasks such as remote-controlled drug and cell delivery and minimally invasive surgery. This work demonstrates the formation of biohybrid sperm-templated clusters under the influence of an external magnetic field and essential functionalities for wireless actuation and drug delivery. Ferromagnetic nanoparticles are electrostatically assembled around dead sperm cells, and the resulting nanoparticle-coated cells are magnetically assembled into three-dimensional biohybrid clusters. The aim of this clustering is threefold: First, to enable rolling locomotion on a nearby solid boundary using a rotating magnetic field; second, to allow for noninvasive localization; third, to load the cells inside the cluster with drugs for targeted therapy. A magneto-hydrodynamic model captures the rotational response of the clusters in a viscous fluid, and predicts an upper bound for their step-out frequency, which is independent of their volume or aspect ratio. Below the step-out frequency, the rolling velocity of the clusters increases nonlinearly with their perimeter and actuation frequency. During rolling locomotion, the clusters are localized using ultrasound images at a relatively large distance, which makes these biohybrid clusters promising for deep-tissue applications. Finally, we show that the estimated drug load scales with the number of cells in the cluster and can be retained for more than 10 h. The aggregation of microrobots enables them to collectively roll in a predictable way in response to an external rotating magnetic field, and enhances ultrasound detectability and drug loading capacity compared to the individual microrobots. The favorable features of biohybrid microrobot clusters place emphasis on the importance of the investigation and development of collective microrobots and their potential for *in vivo* applications.

1. Introduction

Microrobots have the potential for numerous biomedical *in vivo* applications, such as remote-controlled drug and cell delivery [1] and minimally invasive surgery [2, 3]. The ability of these untethered microrobots to access hard-to-reach locations is promising, but multiple hurdles need to be overcome. Among these hurdles, remote actuation, non-invasive localization, and biocompatibility are some of the most challenging from an implementation perspective, as they have to be addressed simultaneously and their trade-offs must be quantified [3, 4]. The small scale of microrobots limits the use of built-in power sources and actuators. Therefore, various external power sources on the microscale have been proposed, such as magnetic fields [5–7], optical energy [8, 9], ultrasound waves [10, 11], chemical reactions [12, 13], and combinations of some of these stimuli [14]. Magnetic fields are particularly promising for

in vivo settings, as they allow for remote, long-range and biocompatible actuation. The magnetic field and gradient can exert sufficient force and torque on microrobots, enabling six-degrees-of-freedom motion [5, 6, 15–22]. In order to not only actuate, but also localize and track the motion of the microrobot in an *in vivo* setting, the magnetic actuation needs to be combined with an imaging modality [23–25]. For the localization of microrobots, existing medical imaging modalities such as photoacoustic computed tomography [26], positron emission tomography [27], magnetic resonance imaging [28], photoacoustic imaging [29], and ultrasound [30] have been explored. Each of these medical imaging modalities has different requirements, such as sufficient contrast agents, echogenicity or the presence of radioactive agents. Among these techniques, ultrasound imaging is a potential option for noninvasive localization and has been established as a standard clinical diagnostic tool. It is radiation-free and provides real-time imaging, allowing for microrobot tracking [31–34]. For *in vivo* applications, the microrobots should be biocompatible. Materials with a high level of biodegradability are the ideal choice, because they do not have to be retrieved after use, nor do they accumulate in organs and trigger chronic inflammatory responses [35]. Biohybrid microrobots, which consist of biological and synthetic components, offer this functionality. The biohybrid integration provides additional advantages, such as adaptability to physiological environment, facile cargo loading, and efficient motion on the microscale [36].

Recently, biohybrid microrobots based on bacteria [28, 37–39], algae [40], cardiomyocytes [41], and sperm cells [42–44] have been developed to offer enhanced biocompatibility and motion under physiological conditions. For example, spermatozoa have been explored as templates for flexible magnetically actuated microrobots [45] due to their intrinsic flexibility and drug loading capacity. Coating the flexible body of sperm cells with magnetic particles enables magnetic actuation, and at the same time increases the echogenicity of the cells to allow for ultrasound imaging [45]. Furthermore, loading the biotemplated microrobots with anticancer drugs has also been demonstrated, which is an essential step in producing microrobots with some basic functionalities.

For practical biohybrid microrobotic systems it is necessary to achieve further improvements in terms of locomotion efficiency, localization, and drug loading capability, before they can be used for targeted drug delivery. The locomotion velocity of individual microrobots is limited by the maximum generated propulsive thrust. The individual microrobots can hardly be localized *in vivo* due to the spatial resolution and contrast-to-noise ratio of existing medical imaging modalities. Additionally, due to its volume, a single microrobot can carry a limited amount of drugs. To achieve a relevant therapeutic outcome by the action of microrobots, research should move toward a greater degree of collaborative and collective behavior of the individual microrobots. Combining several magnetic microrobots into a cluster results in a larger amount of magnetic material and thus increases the magnetic moment, so that a greater magnetic torque can be exerted compared to a single microrobot. Self-assembly of microrobots also introduces new forms of actuation, such as rolling on a surface when they form a three-dimensional geometry [46]. Further, a greater detectable signal for noninvasive localization can be produced, and a greater volume of drug can be loaded and transported.

Concerted robot action is not only important in biohybrid robotic implementation but is inspired by processes in nature. Collective behavior of individual organisms or cells has been observed in many biological systems, such as the flocking of birds, schooling of fish, swarming of bacteria, and clustering of worms [47, 48]. Sperm cells, in particular, show collective behavior to adapt to their surroundings [49]. Simple microrobots in the shape of spheres [50, 51] or disks [52] have been magnetically actuated to show collective behavior and to merge, split, and reshape. Liquid metal rods have been acoustically actuated to provide a similar response to those of the spheres and disks [53]. Microrobot swarms can follow trajectories [54], collaborate in potential additive manufacturing applications [55], transport cargo [56], and are functional in bio-fluids [57]. Besides synthetic microrobots, swarms of magnetotactic bacteria have been steered through vascular structures [58] and used in micro-assembly tasks [28]. These studies show that microrobot clusters improve on the capabilities of individual microrobots.

This study aims to combine the distinct advantages of biohybrid microrobots with those of their collective behavior, to address several practical hurdles for microrobots in targeted drug delivery applications. We investigate the collective behavior of nanoparticle-coated sperm cells [45, 59], which we refer to as IRONSperm (figure 1(A)), under the influence of a rotating magnetic field. Theoretical magneto-hydrodynamic models are developed to understand IRONSperm clustering and cluster motion in a viscous fluid. Clusters of the biohybrid microrobots (figure 1(B)) are formed through electrostatic and magnetic self-assembly and entanglement. These clusters are actuated to study their rotational dynamics and rolling locomotion under the influence of rotating magnetic fields. Finally, drug loading of the IRONSperm clusters with doxorubicin hydrochloride (DOX-HCl) is investigated (figure 1(C)), and noninvasive localization using ultrasound imaging is demonstrated (figure 1(D), video S1 in supplementary material). While the ultrasound localization of IRONSperm clusters has been demonstrated before [45], this study improves the

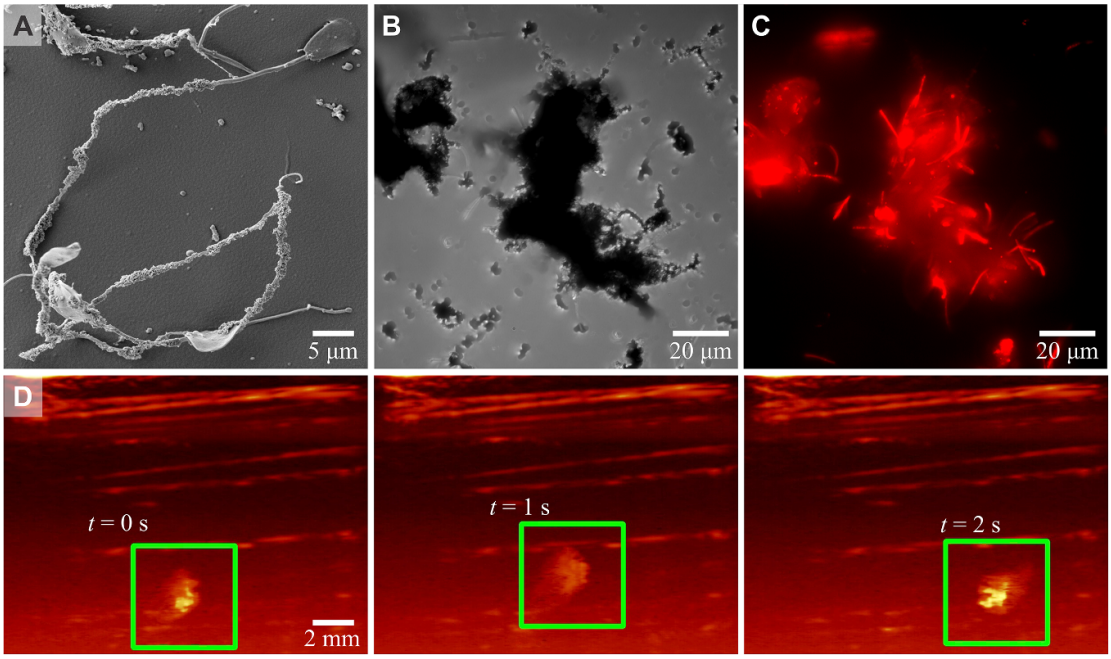

Figure 1. Biohybrid IRONSperm clusters consist of dead bovine sperm cells, coated with iron nanoparticles. (A) Scanning electron micrograph of several entangled IRONSperm samples, the fundamental building blocks of the clusters. (B) Bright-field image of an IRONSperm cluster. (C) Fluorescent image of doxorubicin hydrochloride (DOX-HCl)-loaded IRONSperm cluster. The cancer drug DOX-HCl, which has been taken up by the sperm cells, emits a fluorescent signal and thereby makes the sperm cells visible. (D) Due to their nanoparticle coating, IRONSperm clusters reflect detectable ultrasound waves. In the ultrasound images, the cluster (green square) is pulled by a magnetic field gradient.

localization in multiple ways. First, ultrasound localization is implemented while simultaneously actuating the cluster magnetically, instead of moving by background fluid. Second, the clusters are localized at a significantly larger distance and using a lower ultrasound wave frequency, allowing localization at relatively deep distances.

2. Cluster formation by electrostatic self-assembly and magnetic attraction

A suspension of dead bovine sperm cells and iron nanoparticles self-assembles into IRONSperm, due to the electrostatic forces between the negatively charged sperm cell membranes and the positively charged nanoparticles (figure 2(A)) [60]. Some IRONSperm entangle due to physical interactions, forming clusters (figure 2(B)). These clusters and individual IRONSperm samples are further aggregated using an external magnetic field. Note that the distribution of the nanoparticles along the organic body varies from cell to cell, and depends on the surface charge of each sperm cell. Therefore, an IRONSperm cluster is likely to consist of heterogeneous samples as demonstrated in figure 3. This heterogeneity will affect the electrostatic and magnetic interactions between the individual samples. Note also that the size of the cluster depends on the concentration of sperm cells and nanoparticles, self-assembly time, and magnetic field strength. These fabrication variables can be varied to yield clusters with different sizes. Consider, for example, the fabrication sequence in figure 2 with relatively low concentration of sperm cells and nanoparticles. In this case, the attractive magnetic forces between small clusters might not be large enough to enable them to attract each other. Alternatively, increasing the applied field strength on the same small clusters directly increases the induced magnetic moment and the attractive force. In a magnetic field $\mathbf{B}$, the soft-magnetic IRONSperm clusters are magnetized to a magnetic moment $\mathbf{m}$ (figure 4(A)). At low field strengths, the magnetic moment increases linearly with the field strength (section 9.2 and figure S2 in supplementary material). The magnetic coercivity (for the demagnetizing field) of the clusters is 41 mT. The direction of a cluster's magnetic moment is dependent on the magnetic field direction θ_f, the cluster orientation θ_c, the demagnetizing factor n_a in the preferred magnetization direction of the cluster $\mathbf{e}_1$, and the demagnetizing factor n_r in the direction $\mathbf{e}_2$, perpendicular to $\mathbf{e}_1$, as shown in figure 4(A).

When applying a uniform magnetic field in a low Reynolds number environment far from any solid boundary, the translational motion of a magnetized IRONSperm cluster is governed by the viscous drag force, $\mathbf{F}_d$, and the magnetic force, $\mathbf{F}_m$, exerted by surrounding clusters, such that $\mathbf{F}_d + \mathbf{F}_m = 0$. The viscous drag force is given by $\mathbf{F}_d = -f_t\mathbf{v}$, where f_t is the translational drag coefficient of the cluster and $\mathbf{v}$ is its

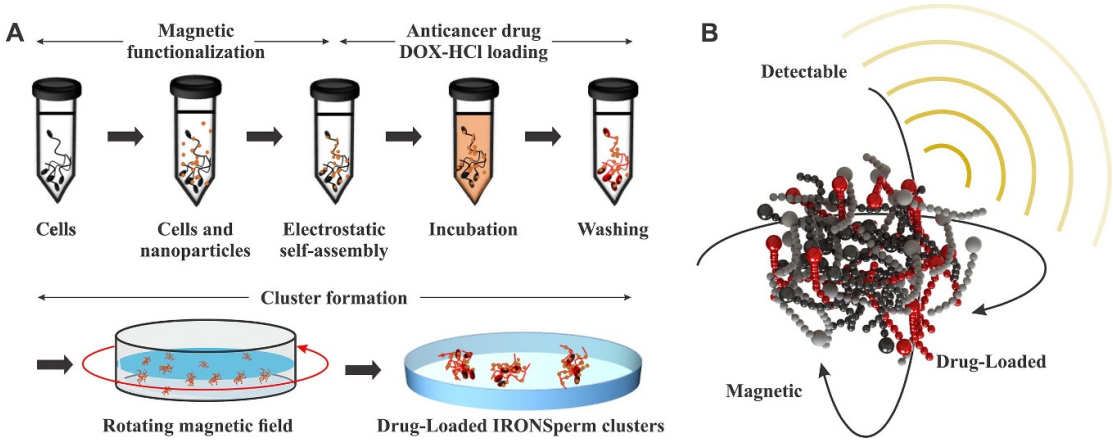

Figure 2. Biohybrid IRONSperm clusters are produced and magnetically functionalized for wireless actuation, noninvasive localization, and drug loading. (A) Nanoparticles are electrostatically assembled around bovine sperm cells. The resulting microrobots are loaded with doxorubicin-hydrochloride (DOX-HCl), and magnetically attracted to form IRONSperm clusters, using a rotating magnetic field. (B) IRONSperm clusters can reflect a detectable ultrasound wave, align with an external magnetic field, and carry drug cargo.

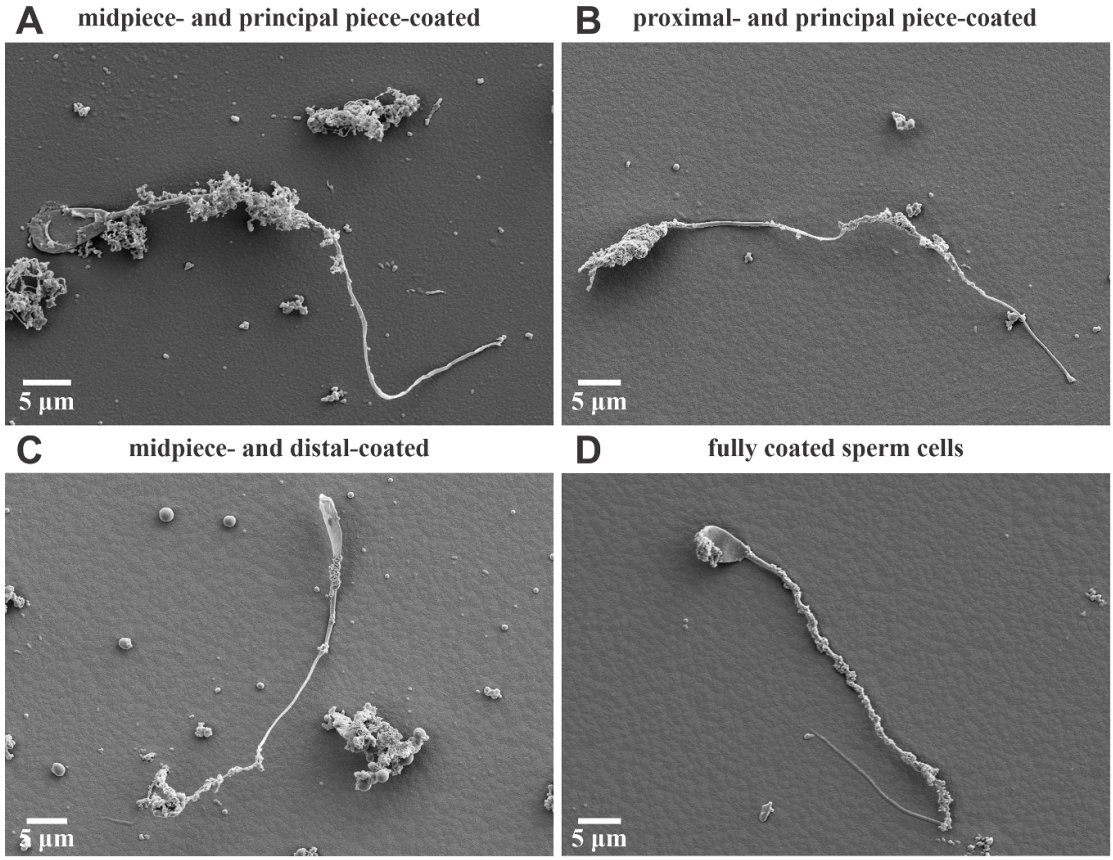

Figure 3. The surface charge of sperm cells vary along the length and has important consequence on the location of the nanoparticles. (A) Midpiece- and principal-piece coated cell. (B) Proximal- and principal piece-coated cell. (C) Midpiece- and distal-coated cell. (D) Fully coated cell.

velocity. The magnetic force that a cluster with magnetic moment $\mathbf{m}_1$ exerts on a neighboring cluster with a magnetic moment $\mathbf{m}_2$ is given by [61]:

$$\mathbf{F}_{\mathrm{m}} = \frac{3\mu_0}{4\pi|\mathbf{r}|^4}\left(\mathbf{m}_2\left(\mathbf{m}_1\cdot\hat{\mathbf{r}}\right)+\mathbf{m}_1\left(\mathbf{m}_2\cdot\hat{\mathbf{r}}\right)+\hat{\mathbf{r}}\left(\mathbf{m}_1\cdot\mathbf{m}_2\right) - 5\hat{\mathbf{r}}\left(\mathbf{m}_1\cdot\hat{\mathbf{r}}\right)\left(\mathbf{m}_2\cdot\hat{\mathbf{r}}\right)\right), \quad (1)$$

where $\hat{\mathbf{r}}$ is the unit vector between the clusters and $|\mathbf{r}|$ is the distance between them (figure 4(B)). Note that the force decreases with the fourth power of the distance between the clusters (i.e. $|\mathbf{F}_{\mathrm{m}}| \sim |\mathbf{r}|^{-4}$). This means that the time for neighboring clusters to reach each other scales with the fifth power of the distance between them [62]. Magnetic attraction is therefore

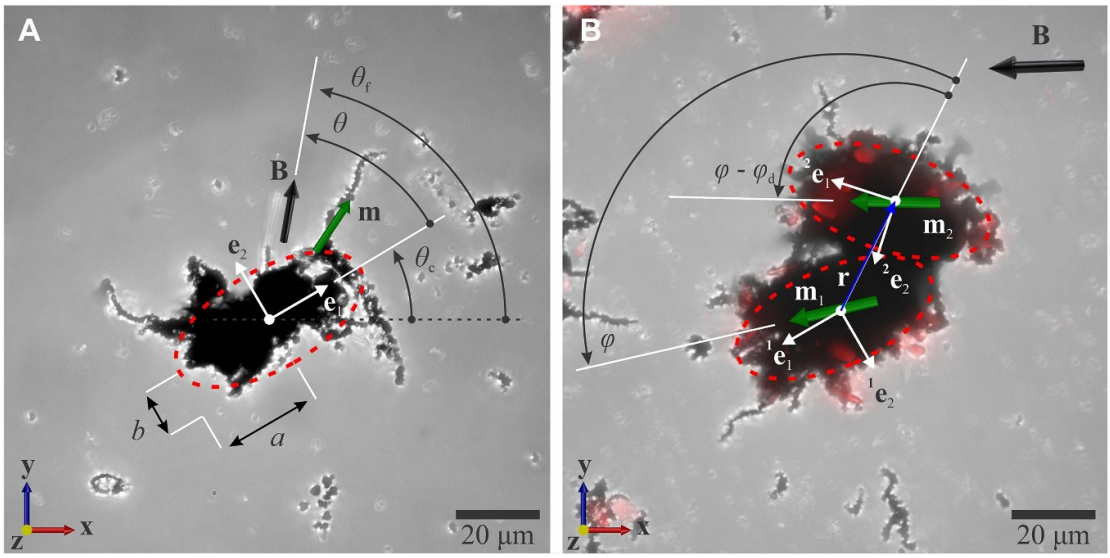

Figure 4. Clusters are approximated as ellipsoids. (A) An external magnetic field, **B**, magnetizes the cluster to a magnetization **m**, depending on the demagnetizing factors of the cluster. (B) Two clusters separated by **r** aggregate in a rotating magnetic field, leading to the formation of a larger cluster. The remanence magnetization and entanglement enable the two clusters to remain attached when the magnetic field is removed.

only suited for relatively short distances and makes the resulting cluster shape and size dependent on the concentration of the nanoparticles and nanoparticle-coated sperm cells in the suspension.

For rotating magnetic field, a common behavior for the the clusters is to trail behind the field, as they attempt to align their preferred magnetization axis with the field. When two neighboring clusters rotate in sync with an external magnetic field, the average attractive force between them per field rotation is given by:

$$\frac{1}{2\pi}\int_0^{2\pi}\mathbf{F}_\mathrm{m}\cdot(-\hat{\mathbf{r}})\mathrm{d}\varphi=\frac{3\mu_0|\mathbf{m}_1||\mathbf{m}_2|}{8\pi|\mathbf{r}|^4}\cos(\varphi_\mathrm{d}),\quad(2)$$

where φ is the angle between $\mathbf{r}$ and $\mathbf{m}_1$, and φ_d is the angle between $\mathbf{m}_1$ and $\mathbf{m}_2$, such that $-\pi/2\leqslant\varphi_\mathrm{d}\leqslant\pi/2$. This force is positive for all possible values of φ_d, causing the clusters to aggregate. A rotating magnetic field is used to form clusters. Further aggregation of these clusters in a rotating magnetic field is likely to yield ellipsoidal structures (video S3 in supplementary material). The attractive magnetic force between neighboring clusters is only noticeable at distances less than a few times their sizes, as expected based on (2). Clusters come in contact (figure 4(B)) and preserve a stable configuration even when the external magnetic field is removed, due to their remanence magnetization and entanglement. Therefore, the clusters may be regarded as connected rigid structures. During fast rotations, the clusters can deform or even break into smaller bodies. In contrast to the cluster, the electrostatic forces between the sperm cells and the nanoparticles are extremely strong, leading to permanent attachment as shown in figure 3. The magnitude of the attractive electrostatic force is proportional to the product of the charges and inversely proportional to the square of the distance between them. Therefore, the attractive electrostatic force between the particles and the cell is much greater than any other forces such as the hydrodynamic drag forces and the contact forces with other cells or a solid boundary.

3. Characterization of the step-out frequency

A magnetic field exerts a torque on an IRONSperm cluster, $\boldsymbol{\tau}_\mathrm{m}=\mathbf{m}\times\mathbf{B}$. Similarly to the force balance, in a low Reynolds number environment the magnetic torque is balanced by the viscous drag torque, $\boldsymbol{\tau}_\mathrm{d}=f_\mathrm{r}\boldsymbol{\omega}_\mathrm{c}$, where f_r is the rotational drag coefficient of the cluster and $\boldsymbol{\omega}_\mathrm{c}$ is its angular velocity, such that $\boldsymbol{\tau}_\mathrm{m}+\boldsymbol{\tau}_\mathrm{d}=0$. Clusters rotate to align their magnetic moment, often in the direction of their longest axis, with the magnetic field. In a uniform rotating magnetic field, the rotational dynamics of magnetic dipoles is given by the following differential equation:

$$\omega_\mathrm{c}=\frac{\mathrm{d}\theta_\mathrm{c}}{\mathrm{d}t}=\begin{cases}\omega_\mathrm{so}\sin(\omega_\mathrm{f}t-\theta_\mathrm{c}), & \text{permanent magnet,}\quad(3a)\\ \omega_\mathrm{so}\sin(2(\omega_\mathrm{f}t-\theta_\mathrm{c})), & \text{soft magnet,}\quad(3b)\end{cases}$$

where ω_so $(\mathrm{rad\,s^{-1}})$ is the step-out frequency, ω_f is the angular velocity of the magnetic field, and t is time. The step-out frequency is the maximum angular velocity at which a cluster rotates in synchrony with the external field, and differs for each cluster

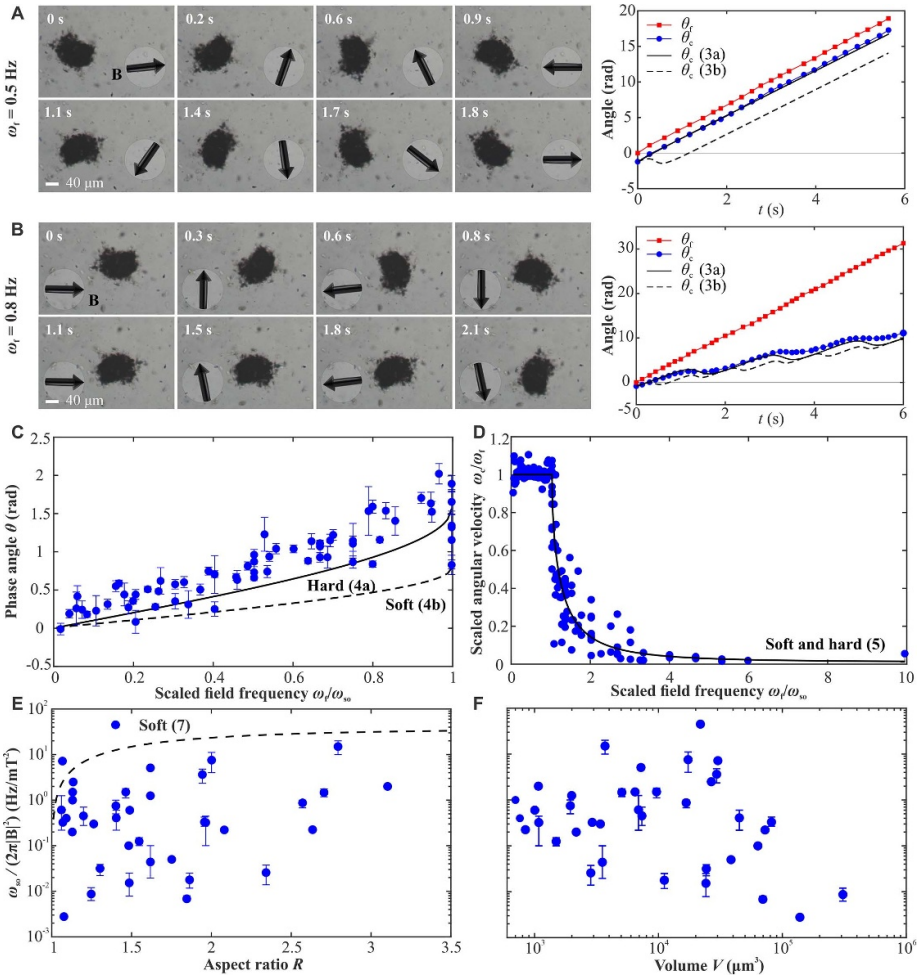

Figure 5. Motion characteristics of IRONSperm clusters. (A) A cluster is actuated below ω_{so} to follow an external magnetic field of 8 mT (black arrow) rotating at 0.5 Hz with a constant phase angle between the field and $\mathbf{e}_1$. The permanent magnet model resembles this cluster movement (right). θ_f is the field direction and θ_c is the cluster direction. (B) A cluster actuated above ω_{so} oscillates under the influence of a rotating field at 0.8 Hz. The phase angle between the field and the cluster orientation is not constant. The permanent magnet model resembles the cluster movement (right). θ_f is the field direction and θ_c is the cluster direction. (C) The phase angle θ between the field and $\mathbf{e}_1$ of the clusters increases with ω_f and is larger than the angle predicted by the soft and hard (permanent) magnet models. The error bars indicate the standard deviation of the phase angle over multiple field rotations ($n = 18$). (D) The average angular velocity of clusters ($n = 27$) is equal to the field angular velocity ω_f up to ω_{so}. Above ω_{so}, the average angular velocity of a cluster decreases with ω_f, in agreement with the soft and hard magnet models. (E) The scaled step-out frequency $\omega_{so}/|\mathbf{B}|^2$ of the clusters shows no relation to the aspect ratio R of the clusters ($n = 38$). Each dot represents the mean scaled step-out frequency of a cluster. If error bars are drawn, these indicate the range of scaled step-out frequencies measured at different field strengths. The step-out frequency predicted by the soft magnet model is larger than 95% of the measurements. (F) The scaled step-out frequency is independent of the estimated volume of the clusters, which is in agreement with the soft and hard magnetic model. Each dot represents the mean scaled step-out frequency of a cluster. If error bars are drawn, these indicate the range of scaled step-out frequencies measured at different field strengths ($n = 38$).

based on its magnetic moment and viscous drag coefficient. Figure 5(A) shows the response of a cluster under the influence of a rotating magnetic field (black arrow) at a frequency of 0.5 Hz. The external magnetic field magnetizes this cluster to magnetization **m**, which allows for rotation in synchrony with the field (video S4 in supplementary material). There is a constant phase angle between the magnetic field and the cluster, which is captured by the permanent magnet model. When actuated above their step-out frequency, clusters undergo oscillations superimposed on the rotational motion (figure 5(B), video S4 in supplementary material), as the cluster can no longer rotate in synchrony with the field rotations. Figure 5(B) shows that these oscillations are captured by the permanent magnet model, as the clusters are actuated below their coercivity field strength.

Below the step-out frequency, the phase angle θ, i.e. the angle between the preferred magnetization direction of an object and the magnetic field during field rotations, increases with the angular velocity of the field, such that:

$$\theta = \begin{cases} \arcsin\left(\frac{\omega_f}{\omega_{so}}\right), & \text{permanent magnet,} \quad (4a) \\ \frac{1}{2}\arcsin\left(\frac{\omega_f}{\omega_{so}}\right), & \text{soft magnet.} \quad (4b) \end{cases}$$

Figure 5(C) shows that the phase angle of the clusters increases with the angular velocity, ω_f, of the field. The permanent magnet model captures the phase

difference between the cluster and the field. However, the measured phase angles are greater than the calculated results of the model. This difference is attributed to the direction of the magnetic moment. While the preferred magnetization direction is measured in a DC field, the shape, and thereby the magnetic moment, of the clusters change slightly due to the viscous drag force when the clusters start to rotate.

As the clusters oscillate when they are actuated above their step-out frequency, their average angular velocity decreases. For both permanent and paramagnetic objects [63, 64], the average angular velocity is given by:

$$\frac{\omega_c}{\omega_f} = 1 - \sqrt{1 - \left(\frac{\omega_{so}}{\omega_f}\right)^2}. \tag{5}$$

Figure 5(D) shows that (5) captures the behavior of the clusters in terms of their average angular velocity. Below the step-out frequency, no oscillations are present and the angular velocity of the cluster is equal to the angular velocity of the magnetic field. Above the step-out frequency, the angular velocity of the clusters decreases rapidly, to less than 20% of the angular velocity of the field at twice the step-out frequency.

The step-out frequency required to model the movement of a cluster is measured experimentally. For permanently magnetic objects, their step-out frequency is given by $\omega_{so} = |\mathbf{m}||\mathbf{B}|/f_r$. However, the magnetization of the individual clusters is unknown. Ideally, the step-out frequency is predicted based on the properties of the cluster. To find an expression for the step-out frequency of a cluster, the cluster is approximated as a soft-magnetic ellipsoid (figure 4(A)). The step-out frequency is then given by [65]:

$$\omega_{so} = \frac{|\mathbf{B}|^2 |n_a - n_r| V}{2\mu_0 n_a n_r f_r}, \tag{6}$$

where V is the volume of the ellipsoid and μ_0 is the permeability of free space. The step-out frequency scales with the square of the field strength. Note that the demagnetizing factors [66] and the rotational drag coefficient [67] of a prolate ellipsoid rotating about one of its radial axes are known. Substitution of these coefficients into (6) shows that the step-out frequency is independent of the volume of the ellipsoid, and solely dependent on the ratio between its axis of symmetry and its radial axes $R = a/b > 1$, such that:

$$\frac{\omega_{so}}{|\mathbf{B}|^2} = \frac{|n_a - n_r|}{16\eta\mu_0 n_a n_r} \frac{(4R^3 - 2R)\ln\left(R + \sqrt{R^2 - 1}\right) - 2R^2\sqrt{R^2 - 1}}{(R^4 - 1)\sqrt{R^2 - 1}}, \tag{7}$$

where η is the viscosity of the surrounding fluid. Figure 5(E) shows the step-out frequency, scaled with the square of the applied field strength as dictated by (7), versus the aspect ratio R of the clusters. Scaling the step-out frequency with the square of the field strength results in an average normalized root-mean-square error (NRMSE) of 31% within a cluster. No correlation between R and the scaled step-out frequency is found. The scaled step-out frequency differs by a factor $\mathcal{O}(10^3)$ between clusters, and the step-out frequency of a cluster could differ slightly. One possible explanation for these findings is that clusters have different step-out frequencies due to their different magnetic moments and viscous drag coefficients. The volume, orientation, and distribution of the nanoparticles determine the magnetic moment of a cluster. Additionally, the geometry and orientation of the cluster, and effects of the environment, such as the effect of a nearby surface [68–70] or fluid heterogeneity, determine the viscous drag experienced by a cluster. The lack of correlation between R and the step-out frequency, can also be explained by the permanent magnet model, which does not dictate a relationship between R and the step-out frequency. Further, measurements show that 95% of the clusters have a step-out frequency below the soft-magnetic model prediction, for $\eta = 0.001$ Pa s. While the model assumes a solid paramagnetic ellipsoid, the IRONSperm clusters consist of ferromagnetic nanoparticles and sperm cells, resulting in a much less magnetic material. Figure 5(F) shows that there is no relation between the estimated volume of a cluster and its scaled step-out frequency. This behavior is also predicted by both the soft- and permanent-magnet models, as the drag coefficient of an object and the amount of magnetic material both increase with the volume.

4. Rolling velocity of the clusters

The rotational motion of a cluster in a rotating magnetic field can be used for locomotion. As it is likely that a cluster is close to a boundary, rolling is a convenient locomotion mechanism. When a cluster is in contact with a surface, applying a magnetic field rotating about an axis in the x–y plane causes the cluster to roll. In this case, a relatively large cluster

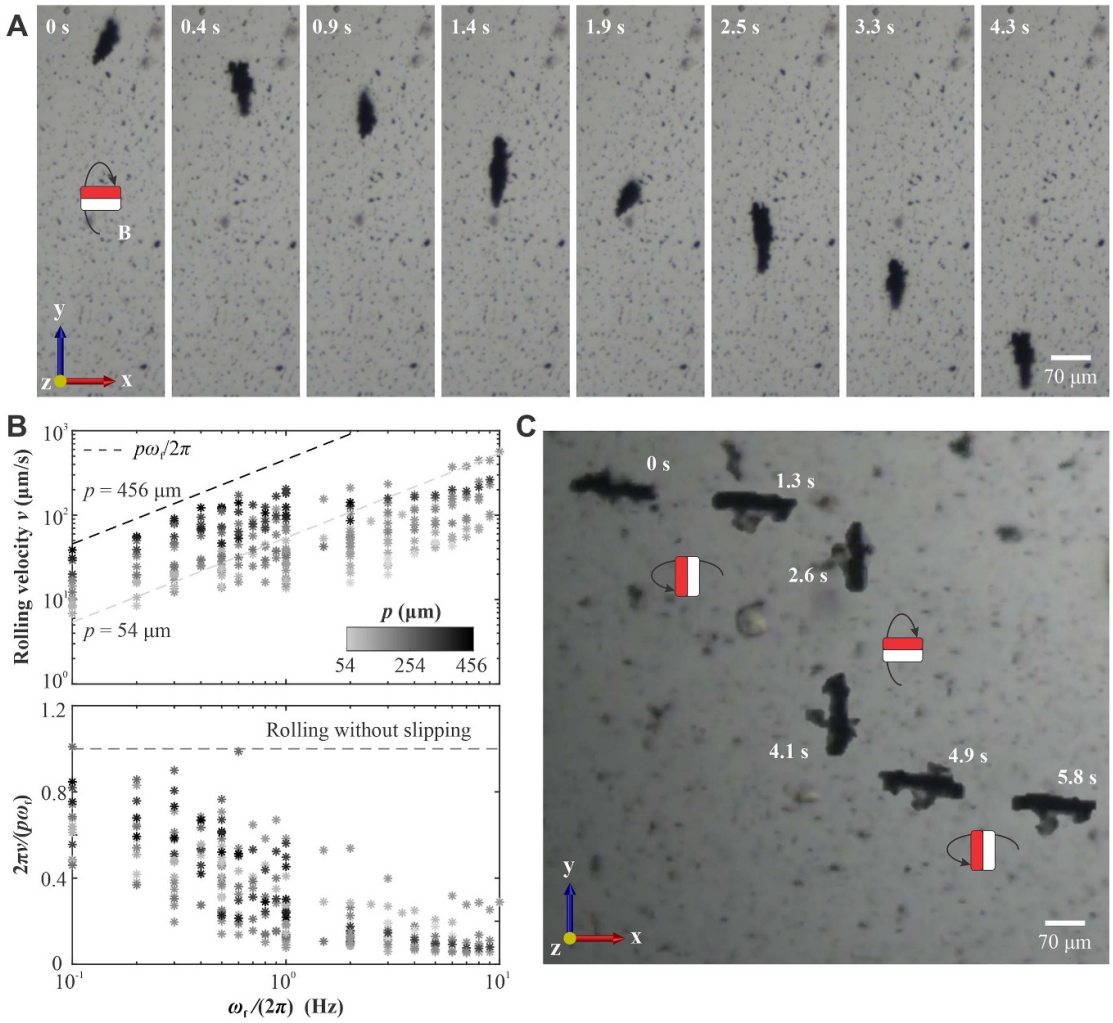

Figure 6. IRONSperm clusters can roll over a surface and can be steered by controlling the field-rotation axis in the *x*–*y* plane. (A) An IRONSperm cluster rolls on a surface at a velocity of 110 µm s^{-1} under the influence of a magnetic field of 4 mT rotating at 0.5 Hz about the *x*-axis. (B) Top: The rolling velocity of the clusters increases non-linearly with frequency. Larger clusters roll faster than smaller clusters at the same actuation frequency ($n = 35$). Bottom: The number of perimeters traveled per field rotation decreases with actuation frequency ($n = 35$). (C) By changing the field-rotation axis, the cluster is steered to roll along a prescribed path. The cluster changes direction with approximately 9 rad s^{-1}. The cluster moves at 140 µm s^{-1} as it is actuated by a 6 mT magnetic field rotating at a frequency of 3 Hz.

can break into smaller clusters at relatively high actuation frequencies. Figure 6(A) shows a cluster rolling as the magnetic field rotates about the *x*-axis (video S5 in supplementary material). During rolling without slipping, an object travels the length of its perimeter p in one rotation, i.e. the rolling velocity v scales linearly with the perimeter of the object and the actuation frequency, such that $v = p\omega_f/(2\pi)$. The top graph in figure 6(B) shows that the rolling velocity of the clusters increases linearly with the actuation frequency up to approximately 0.4 Hz. Above this value, the rolling velocity further increases nonlinearly. Clusters with a larger perimeter move faster than clusters with a smaller perimeter at the same actuation frequency. A maximum rolling velocity of 563 µm s^{-1} is achieved by a cluster with an estimated circumference of 195 µm under the influence of actuating field at frequency of 10 Hz. The bottom graph in figure 6(B) shows that the rolling velocity scaled by the actuation frequency and cluster perimeter, i.e. the number of perimeters traveled by a cluster per rotation of the magnetic field, decreases with the actuation frequency. The prediction based on rolling without slipping is an upper limit for the rolling velocity. Only at low frequencies do the clusters approach this limit. We hypothesize that at greater actuation frequencies, the clusters start slipping on the surface. Possibly, hydrodynamic lift is generated at high frequencies [71], such that clusters no longer experience enough traction to roll.

During rolling, the clusters can be steered in 2D space, by changing the rotation axis of the field (figure 6(C), video S6 in supplementary material). At $t = 0$ s, the field is rotating about the *y*-axis at 3 Hz. At $t = 2.4$ s, the field is rotating about the *x*-axis and the cluster turns. As the clusters have a preferred orientation in the magnetic field (section 3), the clusters turn, instead of switching their rotation axis, when

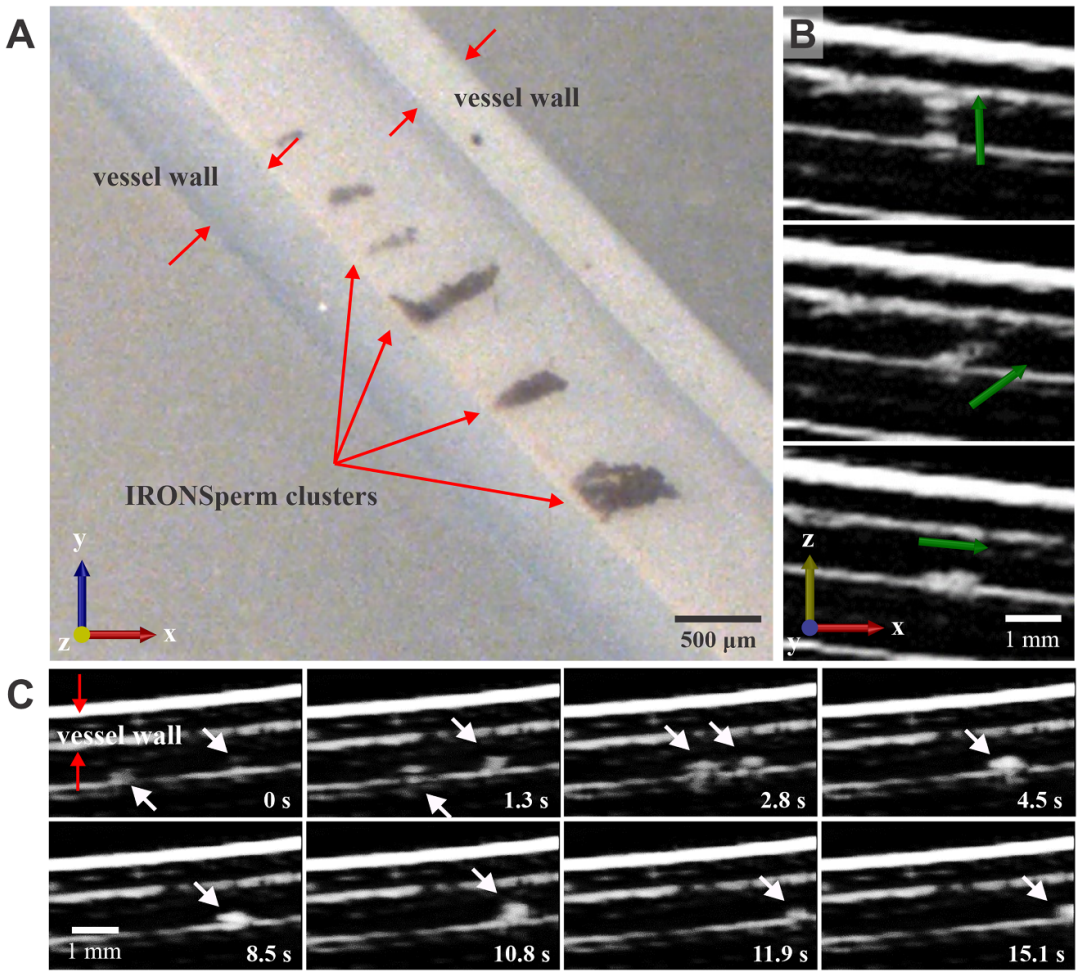

Figure 7. The IRONSperm clusters are localized using ultrasound images. (A) The clusters used during the ultrasound experiments are less than 800 µm in length. Due to clustering their size changed during the experiments. (B) The orientation of this 800 µm long cluster is estimated from ultrasound images within 20° using 14 MHz ultrasound waves at a distance of approximately 0.5 cm. The green arrow represents the magnetization direction. (C) The clusters with a diameter of 500 µm are tracked during magnetic actuation using 14 MHz ultrasound waves at a distance of approximately 0.5 cm. The white arrows indicate the clusters. At $t = 4.5$ s, two IRONSperm clusters merged and continued rolling together. The merge increased their echogenicity by 50%.

changing the rotation axis of the external field. At $t = 4.6$ s, the field is rotating about the y-axis again and the cluster turns. The clusters change direction with up to 9 rad s^{-1}, depending on their magnetic moment and viscous drag coefficient.

In the actuation experiment, we observe that the clusters have greater structural stability at low actuation frequencies. Each motion control trial is performed with a cluster for at least 30 min and therefore they retain their stable structure even under the influence of contact forces during rolling locomotion. Note that these experiments are performed in water with viscosity and density of 1.0 mPa s and 997 kg m^3. Similar properties hold for blood serum with viscosity and density of 1.105 mPa s and 906 kg m^3, respectively. Therefore, the hydrodynamic drag coefficients and the drag forces and torques will be approximately similar in blood serum. Additionally, we observed good stability of the IRONSperm clusters in 10% fetal bovine serum during the cytotoxicity studies.

5. Localization of IRONSperm clusters using ultrasound imaging

The movement of the clusters can be followed easily under a microscope *in vitro*, but *in vivo*, optical imaging modalities cannot be used and instead medical imaging modalities such as ultrasound are required. Ultrasound waves travel through a medium at a velocity c, depending on the density of the medium. When a wave encounters an acoustic impedance mismatch, part of the wave is reflected. Due to the iron nanoparticles in the IRONSperm clusters, the clusters have a different acoustic impedance from their surroundings. Detecting the reflected ultrasound waves makes IRONSperm clusters visible on ultrasound images. The axial resolution of ultrasound imaging is equal to the wavelength, λ, of the used ultrasound waves [72]. This wavelength is given by $\lambda = c/f$, where f is the frequency of the ultrasound waves. In tissue, $c \approx 1540$ m s^{-1}. Therefore, a cluster with a diameter of 500 µm (figure 7(A)), can be detected using an

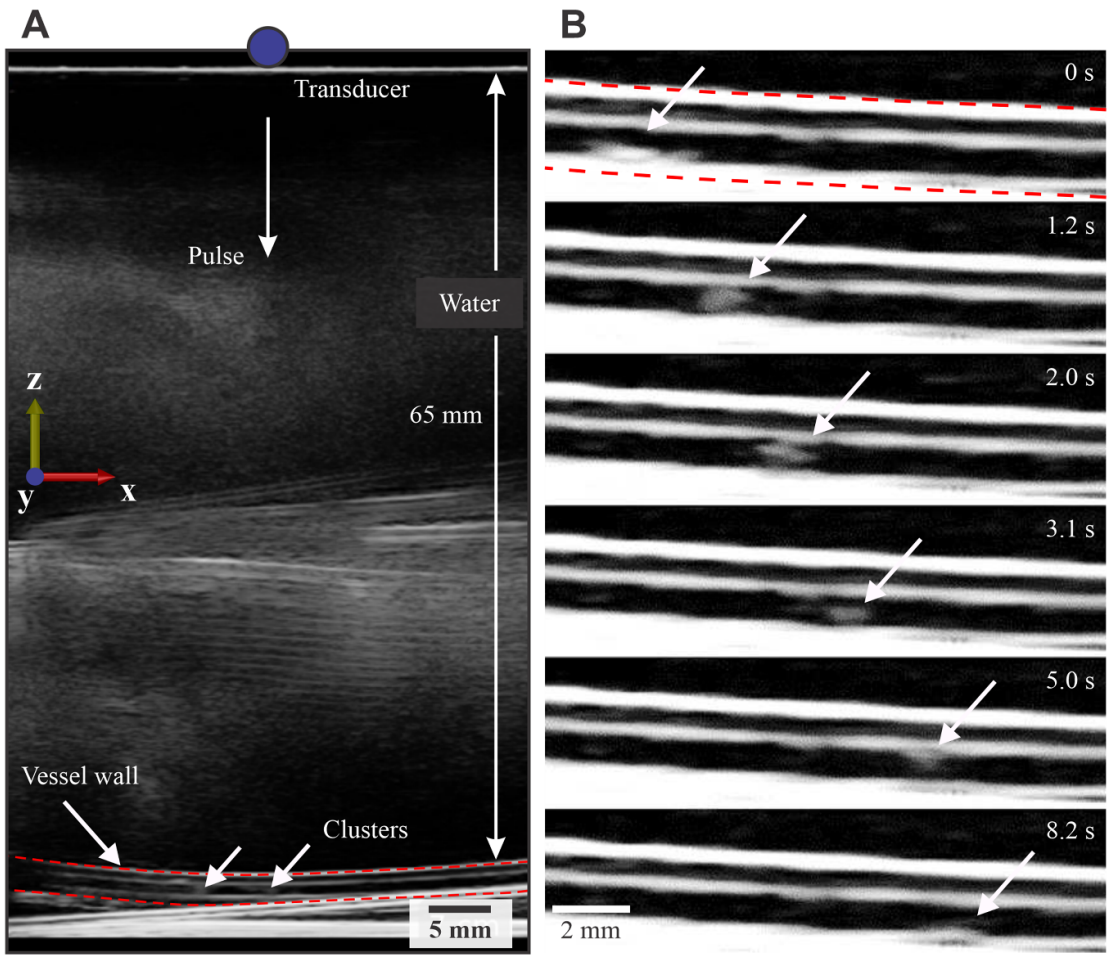

Figure 8. Localization of IRONSperm clusters by ultrasound images is achieved at relatively large penetration depth. (A) The clusters are detectable using 10 MHz ultrasound waves at a distance of approximately 6.5 cm. (B) The clusters are localized during magnetic actuation at a distance of 6.5 cm. The white arrows indicate a cluster rolling at approximately 1 mm s^{-1}, while actuated at frequency of 1 Hz.

ultrasound frequency of at least 3 MHz. From a penetration depth of 5 mm and using an ultrasound frequency of 14 MHz, the orientation of a cluster with a diameter of 800 µm can be estimated within approximately 20° on the ultrasound images (figure 7(B), video S7 in supplementary material). Figure 7(C) shows that the motion and time-varying orientation of the clusters during rolling improves the contrast of the clusters in the ultrasound images. As shown in section 3, clusters can merge and in this case the contrast of the two clusters at $t = 4.5$ s is improved, i.e. pixel intensity, by 50% (video S8 in supplementary material) and the larger resulting size enables easier detectability.

Note that the experimental actuation and localization results shown in figure 7 are achieved with a small distance between the ultrasound transducer and the cluster. For practical medical applications, it is necessary to localize the cluster at greater penetration depths as the microrobots need to access deeper tissues. The penetration depth of ultrasound waves increases with their wavelength [72]. As larger clusters remain visible when a larger ultrasound wavelength is used, larger clusters are detectable at larger depths. Figure 8(A) shows that IRONSperm clusters with a diameter of 500 µm are visible at a distance of 65 mm, the maximum setting of the used ultrasound probe. During this localization trial, the clusters are actuated using a 1 Hz rotating magnetic field to move at approximately 1 mm s^{-1} (video S9 in supplementary material). While the clusters can be followed, the decreased ultrasound frequency of 10 MHz decreases the spatial resolution. The detectability of the clusters is dependent on their orientation with respect to the ultrasound transducer. During rolling, the orientation of the cluster alters continuously, improving detectability of clusters that have an axis which is too short to be detected [73]. To ensure that the cluster is continuously visible during rolling, each axis of the cluster should be long enough to be detectable. This length is dependent on the used ultrasound settings.

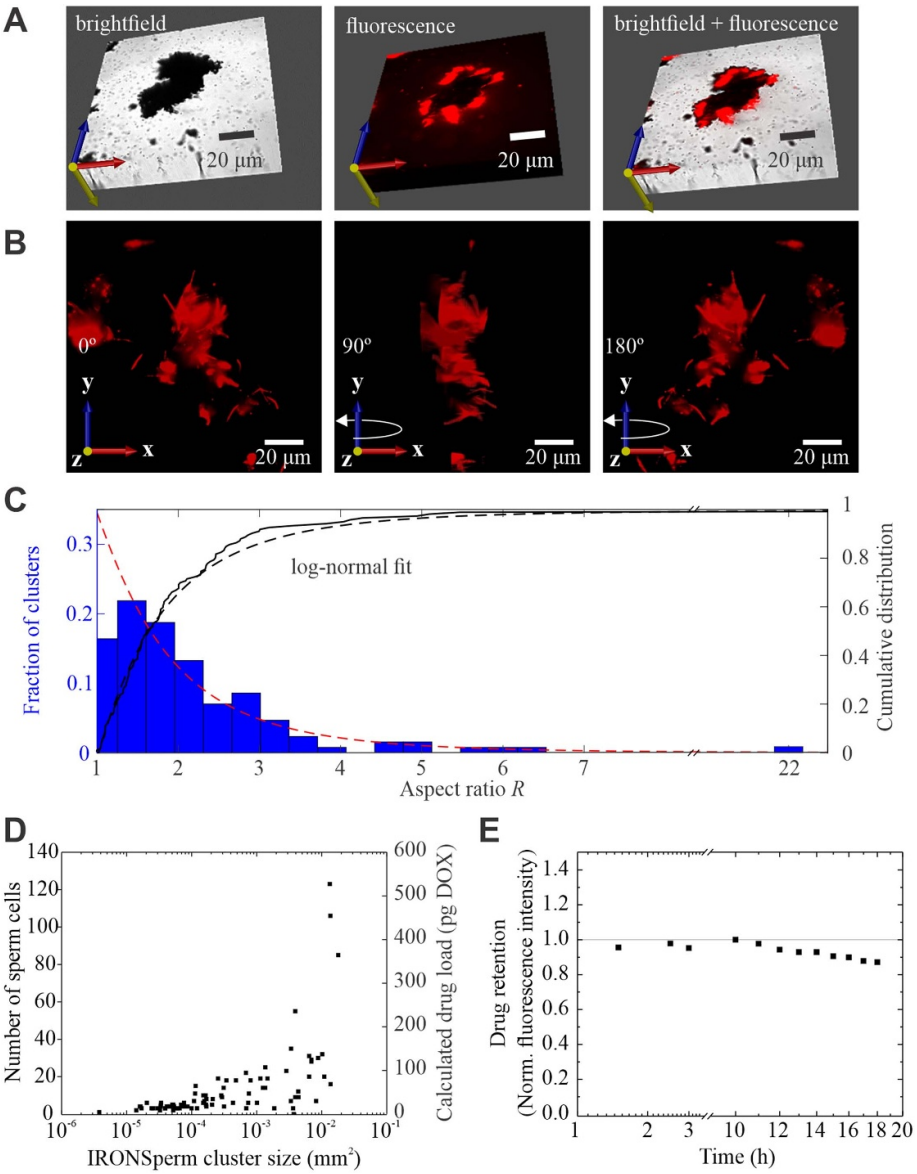

Figure 9. IRONSperm clusters of different shapes and sizes are loaded with drugs. (A) 3D reconstruction of a z-stack of an IRONSperm cluster from bright-field (BF), fluorescent (FL) and BF-FL-overlayed images. (B) 3D reconstruction of an IRONSperm cluster from fluorescent z-stacks (50 slices) from different angles (0°, 90° and 180°). DOX-HCl-loaded bovine sperm appear red in fluorescent channel. The DOX-HCl is distributed over the whole cluster. (C) Distribution of the aspect ratio of clusters ($n = 128$). The red dashed line is a fitted folded log-normal probability density function, scaled to match the histogram. Most clusters have an aspect ratio below 3. (D) Number of cells (left y-axis) and respective calculated drug load (right y-axis) per IRONSperm cluster ($n = 88$). Cluster size was measured by area per 2D image. In general, the number of cells increases with cluster size, but the large spread indicates different cell densities. (E) Drug retention of DOX-HCl-loaded clusters over time. Drugs can be retained for more than 10 h, after which a 20% decrease is seen in the next 10 h.

6. Drug loading and cytotoxicity of the clusters

IRONSperm clusters can be magnetically actuated and localized using ultrasound imaging simultaneously. These are the first steps for the intended *in vivo* biological application. When IRONSperm clusters are incubated with the anticancer drug DOX-HCl, the sperm cells absorb this drug through their cell membrane (figure 2(A)). After one hour of incubation of the nanoparticle-coated sperm cells with this drug, the cells take up an average of 4.29 pg DOX-HCl per cell. This is in agreement with previously reported amounts of drugs per sperm cell [45].

The DOX-HCl is fluorescent, so the drug-loaded sperm cells in the clusters can be visualized using fluorescent microscopy. The cytosol volume of the head is much larger than that of the flagellum, so that the drug is mostly present in the head, visible by the strong fluorescent signal of the sperm heads in the images. These areas in the cluster that contain magnetic nanoparticles, do not contain drugs, and do not emit fluorescent signals, as shown in figures 9(A) and (B), which display 3D reconstructions of two different

clusters. The red dots show the distribution of the drug-loaded sperm cells within the cluster. Note that the cluster in figure 9(A) is a densely packed agglomerate that displays the majority of the drug-loaded sperm cells on the surface of the cluster. The density of the cluster can be recognized by the strong contrast of the cluster in the bright-field image figure 9(A). Here, there is no space between the sperm cells and a higher amount of magnetic particles might have led to the tight packing of the cluster. One reason why fluorescent cells can only be seen in the perimeter of the cluster is that the fluorescent signal from any cells in the center are blocked by the cluster itself. The high density of iron oxide particles in the center of the cluster might lead to quenching of the fluorescent signal of the drug-loaded sperm. On the other hand, this might be due to the mechanism of clustering, which arranges the cell-particle agglomerate in a way that the magnetic material is agglomerated more in the center of the cluster under the influence of the rotating magnetic field, while the cell heads orient toward to outer area of the cluster.

The display of the drug-loaded cells on the surface of the magnetic cluster has the benefit of enhancing the drug availability to the target. In figure 9(B) (video S10 in supplementary material), the 3D reconstruction of another cluster is shown from different angles. It can be seen that the sperm cells and the DOX-HCl are distributed fairly uniformly over the entire cluster. This cluster might contain a lower density of magnetic material and hence did not agglomerate as tightly. In this case, all fluorescent cells are visible throughout the cluster without blocking of the fluorescent signal due to a looser agglomeration of the IRONSperm. We can assume that with increasing exposure to rotating magnetic field, the density of the cluster increases due to prolonged magnetic attraction between the magnetic elements inside the cluster and the interaction with the environment which leads to denser agglomeration. At the same time, more IRONSperm are added to the cluster, so that the size is also increasing over time.

The IRONSperm clusters vary in their shape and size (figure S11 in supplementary material). Their aspect ratio R follows a log-normal distribution with a mode of 1.7 and a standard deviation of 2.1 (figure 9(C), $n = 128$). There are a few clusters with an aspect ratio higher than 4. These are mostly clusters with a few sperm cells (less than 25 cells), so that the aspect ratio of single bovine sperm cell (ca. 1:60) plays a role in the resulting elongated cluster. As shown in section 3, aspect ratio is not important for actuation. However, it could influence the drug release based on the surface area of the cluster. Cluster dimensions vary between 18 and 607 µm ($n = 128$). The importance of cluster size for locomotion is addressed in section 4. For drug loading, cluster size is important because the number of sperm cells increases with cluster size (figure 9(D)). Since the sperm cells are loaded with the drugs prior to clustering, a uniform loading is guaranteed. Hence, the drug load increases approximately proportional to the number of cells in the cluster. However, cell density varies among clusters and this variation increases with cluster size. As the analyzed clusters contained up to 120 sperm cells, theoretically a load of up to 500 pg DOX-HCl per cluster could be achieved. Not only can the clusters be loaded with drugs, the IRONSperm clusters also retain the drugs for up to 10 h (figure 9(E)). This is possible because the biomembrane of the cells takes up the drug easily and contains it stably inside the cytosol. After 10 h, a slight decrease in fluorescence intensity of approximately 2% per hour is observed for the next 10 h. Note that the exact uptake mechanism of the drugs into IRONSperm has not been investigated yet. In our approach, this technique allows us to achieve intracellular loading without considering the biological activity of the cells (no active uptake), since they are only used to carry the drug cargo. In this study, we have tested the capability of the clusters to retain doxorubicin as a standard anti-cancer drug. Similar response is expected with other anti-cancer drugs of similar size and charge.

In order to evaluate the cytotoxicity of IRONSperm clusters, we incubate cervical carcinoma HeLa cells with IRONSperm clusters (drug-loaded and non-drug-loaded) for 42 h. Subsequently we performed a live/dead viability stain on the HeLa cells to evaluate the toxicity of IRONSperm. Figure 10 shows representative images of brightfield, Calcein stained (live, green), and Ethidium homodimer (dead, red) HeLa cells of the control sample (figure 10(A)), HeLa with IRONSperm clusters (figure 10(B)) and HeLa with DOX-HCl-loaded IRONSperm clusters (figure 10(C)). The control sample contains HeLa cells only and shows a viability of 98%. Pure IRONSperm samples show a slightly reduced viability of HeLa cells of 80% which can be attributed to the iron oxide particles. DOX-HCl loaded IRONSperm samples reduced the viability of HeLa cells to 22%, indicating the chemotherapeutic effect of the cancer drug (figure 10(D)). The amounts of IRONSperm samples per HeLa cell need to be optimized to achieve rapid and efficient cancer cell killing.

7. Discussions

Contrary to the non-biohybrid microrobot collectives researched previously [50–57], the IRONSperm clusters do not rely solely on an external input to bundle together. While a magnetic field is used to initially aggregate clusters, the IRONSperm clusters are able to stay connected due to the entanglement and stiction forces between the sperm cells that act as flexible magnetic filaments. The properties of biological cells assist in the control of microrobots [36]. While the biological stiction force eases the formation

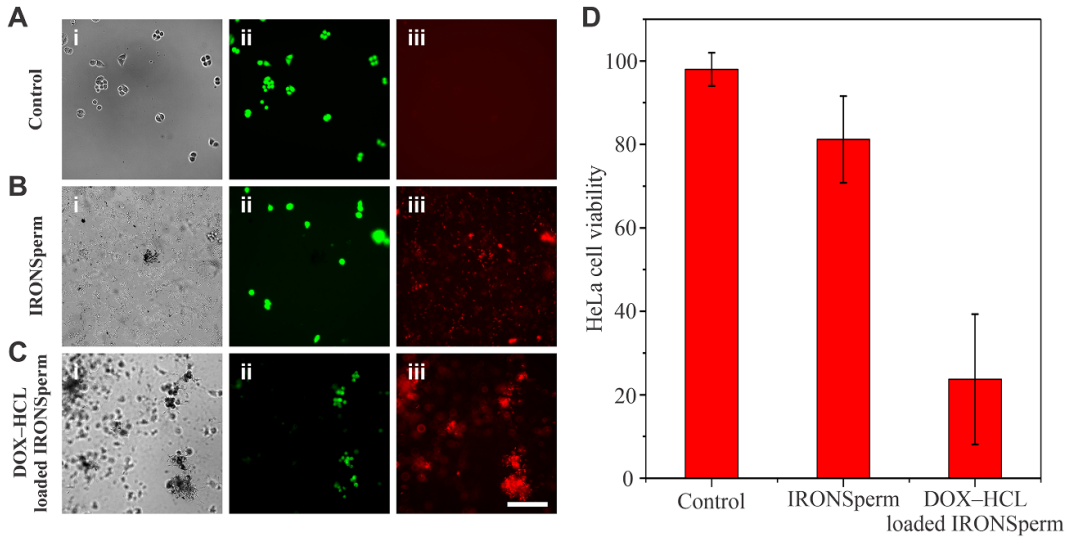

Figure 10. Cytotoxicity of IRONSperm clusters evaluated on HeLa cells after 42 h incubation with IRONSperm. (A) Brightfield, green fluorescent (live) and red fluorescent (dead) images of control samples of HeLa without IRONSperm clusters. (B) HeLa cells incubated IRONSperm clusters. (C) HeLa cells with DOX-HCl loaded IRONSperm clusters. (D) Overall HeLa Cell viability show that DOX-HCl loaded IRONSperm clusters reduce the viability of HeLa cells to about 22%.

of IRONSperm clusters, it also prevents the clusters to reconfigure their structure or even break up into smaller clusters. This ability would be useful to access hard-to-reach locations, as shown with previously developed microrobot swarms [50, 52].

To actuate a cluster, the step-out frequency is determined by finding the frequency at which the cluster start to oscillate. Other measurable parameters, such as the average angular velocity during oscillations [74], the phase angle when moving in sync with the magnetic field, or the oscillation frequency can also be used to find the step-out frequency. However, predicting the step-out frequency based on cluster appearance would be ideal. The paramagnetic ellipsoid model provides an upper bound for the step-out frequency of the clusters, but improved estimates of the drag coefficient and magnetic moment of IRONSperm clusters could lead to more accurate step-out frequency predictions.

Rolling locomotion allows IRONSperm clusters to move at speed of 500 $\mu m\,s^{-1}$, fifty times faster than the swimming velocity of an individual IRONSperm, tackling the disadvantage of slow locomotion speeds of the individual IRONSperm [45]. However, this locomotion strategy requires a surface to roll on, whereas the IRONSperm can swim in the bulk fluid. The achieved rolling velocity is faster than the 300 $\mu m\,s^{-1}$ achieved with magnetotactic bacteria swarms [58, 75], but slower than the 42 $mm\,s^{-1}$ achieved with disk-shaped non-hybrid microrobots of similar size to the IRONSperm clusters [52].

In future work, further measurements of the magnetization, drag coefficient and stiction forces of IRONSperm clusters could provide more accurate predictions of the behavior of IRONSperm cluster. With this knowledge, the building of clusters with specific shapes and sizes, and the reshaping, combining and splitting of clusters can be investigated. Disconnecting individual IRONSperm from the cluster, to actuate IRONSperm to swim instead of roll, could allow for locomotion when no rolling surface is available. The wide range of step-out frequencies among clusters could prove useful for simultaneous actuation of multiple clusters [65] at different rolling velocities under the influence of the same magnetic field. Further, the ability to move through complex environments, such as vasculature and cavities would be of high interest in order to evaluate their *in vivo* application potential. While the actuation of the clusters in this study was done at relatively short distance, stronger magnetic fields could facilitate long-range actuation. The drug retention of IRONSperm clusters is longer compared to liposomes, which usually start releasing up to 30% of the drug over the first two hours [76]. However, compared to liposomes, the drug loading amount of IRONSperm clusters could still be increased. Further work should aim to investigate the optimum concentration and incubation time for effective cancer treatment. Our initial cytotoxicity experiment demonstrated the anti-cancer effect of the DOX-HCl-loaded IRONSperm clusters. Drug release experiments should be performed over longer periods to investigate the role that the cluster size plays on the release time. However, the focus of this article is on the modeling, wireless actuation, and ultrasound imaging of the drug-loaded clusters. Finding the optimum concentration and incubation time is subject of future studies. In addition, loading different types of cancer drugs and different types of cancer tissue is essential to

understand the potential biomedical applications of the clusters. Previous studies have shown that drug-loaded sperm cells are able to fuse with cancer cells and thereby deliver the drug to the cancer cells [11]. It has been shown that this fusion process is relatively slow and regulated by the sperm cell-to-cancer cell interaction. Possible mechanisms are the membrane fusion between the cells or release of drugs when the sperm membrane starts to degrade due to present enzymatic reactions. Controlled drug release mechanisms would complement the drug loading and retention well. Possible approaches to achieve this would be to conjugate the magnetic nanoparticles with cell-specific antibodies, which are then only targeting cells of interest (e.g. cancer cells). In combination with ultrasound, sonoporation, the ultrasound-based permeabilisation of the sperm cell membranes, could also be of interest [77].

Finally, combining living sperm cells with magnetic nanoparticles results in novel explorative microrobotic tools, which could be used for new purposes. It enables the visualization of sperm swarms *in vivo* which is an important tool for the investigation of *in vivo* processes. The ability to make swarms of spermatozoa visible using ultrasound imaging provides a new tool for the study of sperm migration, to understand how long and where sperm cells remain inside the reproductive tract. Currently, such sperm tracking towards the fertilization site is not possible in a non-invasive manner. Besides the application in reproductive science, biohybrid microrobots could be used to act as deep vessel delivery machines or diagnostic tools.

8. Conclusions

In this work, we fabricate drug-loaded biohybrid clusters and understand their characteristics to enable wireless rolling locomotion and noninvasive localization simultaneously. Nanoparticle-coated sperm cells electrostatically and magnetically entangle in dense clusters of up to 120 cells, with dimensions between 20 and 600 µm and cell density variation by an order of magnitude. Despite the cell density variation between clusters and their complex internal structure, the movement of a cluster in a rotating magnetic field is captured by a permanent magnet model, using the step-out frequency of the cluster, owing to the remanence magnetization of the clusters. A soft-magnetic ellipsoid model predicts a step-out frequency of the clusters based on their aspect ratio, but overestimates 95% of the cases. In reality, the step-out frequency of the clusters is independent of the aspect ratio and volume of the clusters. Consequently, permanent magnet models will likely be the best choice in real-time motion control. As proof of concept, the cluster are steered controllably by magnetic actuation below their step-out frequency, and achieve rolling velocities of 500 µm s^{-1} at an actuation frequency of 10 Hz. The rolling velocity increases nonlinearly with the actuation frequency of the field and cluster perimeter. During actuation, the clusters are visible on ultrasound imaging, in contrast to individual IRONSperm. At a distance of 65 mm, clusters with a diameter of 500 µm remain detectable while traveling at 1 mm s^{-1}. A potential application of the IRONSperm clusters is targeted drug delivery. As a demonstration, the sperm cells in the clusters were loaded with DOX-HCl. The largest cluster contained up to 120 cells and could theoretically contain up to 500 pg of DOX-HCl. Based on fluorescence intensity measurements, the drugs were retained for up to 10 h, with a 20% reduction in the next 10 h. The aggregation of drug-loaded microrobots, and their collective actuation and localization potential demonstrated in this study place emphasis on the importance of the investigation and development of collective microrobots and their potential for *in vivo* applications.

9. Materials and methods

9.1. Fabrication of biohybrid IRONSperm

Sperm-templated microrobots were fabricated by an electrostatic-based self-assembly of iron oxide nanoparticles and sperm cells [45]. Cryopreserved bovine semen straws were obtained from Masterrind GmbH Meißen and stored in liquid nitrogen. The semen straws were thawed in a 37 °C water bath for 2 min, before diluting the semen in 1 ml SP-TALP (Caisson labs). The sperm sample containing 3×10^7 cells ml^{-1} was centrifuged at 300 g for 5 min, the supernatant removed and resuspended in distilled water. This washing step was repeated twice before adding the elongated 400 nm long maghemite rice grain-shaped nanoparticles. The diameter of these particles is 150 nm. The sperm cells die in the process and retain a negative surface charge along the length on average. Samples were stored at 5 °C and agglomeration of the cells enables formation of the clusters. Theoretically, the maximum number of nanoparticles per sperm cell can be calculated using the total surface area of a sperm cell (i.e. $\sim 8.5 \times 10^{-10}$ m^2) and the volume of the rice grain-shaped nanoparticles. Assuming that the cell is negatively charged, 14 300 nanoparticles can cover one cell.

9.2. Magnetic moment and step-out frequency characterization

Suspensions of IRONSperm clusters in distilled water with approximately 1.7×10^5 cells ml^{-1} were used to measure the magnetic moment using a vibrating sample magnetometer (VSM) from Oxford Instruments. The suspension is contained inside a plastic container and a polyetheretherketone sample holder. The collected magnetization data (figure S2 in supplementary material) show hysteretic effects within the range of external magnetic field of ±2 T and a magnetic coercivity of 41 mT.

The step-out frequencies of IRONSperm clusters were characterized using a triaxial Helmholtz coil system. The Helmholtz coils generate a maximum magnetic field of 8 mT and maximum rotational frequencies of 10 Hz. Optical images were captured at 30 fps using a microscopic unit (MF-B Series 176 Measuring Microscopes, Mitutoyo, Kawasaki, Japan) and camera (avA1000-120kc, Basler Area Scan Camera, Basler AG, Ahrensburg, Germany). Cluster with various sizes were analyzed using 3×, 10× and 20× Mitutoyo phase objectives. IRONSperm samples of approximately 3 µl were analyzed in this setup. IRONSperm concentrations between approximately 1.2×10^2 and 1.8×10^3 cells µl^{-1} were used. In each trial, existing IRONSperm clusters were localized, or new clusters were formed by applying rotating magnetic field of 8 mT at frequency of 0.1 Hz or by rolling the IRONSperm clusters on the surface to enable agglomeration with a neighboring cluster. The magnetic field-rotation axis was set perpendicular to the surface (figure 4(A), z-axis). An initial field strength was adjusted based on the magnetic response of the cluster. A DC field was applied to determine the preferred magnetization axis of each cluster. The clusters were actuated at a frequency range between 0.1 and 10 Hz until the magnetic torque was no longer sufficient to keep them in synchrony with the field, i.e. the step-out frequency was reached. The actuation frequency was increased with steps of 0.1 Hz. The field strength was increased and again the step-out frequency was measured by increasing the field frequency. The phase angle was measured at approximately ten points in time over a period of multiple cluster rotations to find an average phase angle. The angular velocity of the clusters was measured over multiple field rotations. Step-out frequency characterization data were collected using 38 IRONSperm clusters. Each cluster was traced with an ellipse to estimate its axis lengths and aspect ratio R, as shown in figure 4. The volume of each cluster was estimated using the volume of a prolate ellipsoid, $\frac{4}{3}\pi ab^2$. The phase lag of 18 of the 38 clusters was measured, as the preferred magnetization axes of these clusters were clearly distinguishable. The angular velocity of 27 of the 38 clusters was estimated, as these clusters were actuated at a low enough frequency to prevent aliasing of the used camera.

Differential equation (3) was simulated in MATLAB2019B using the forward Euler method with a timestep of 0.001. For the initial conditions, the values of the first measurement of the field and cluster direction were used.

9.3. Rolling velocity

A field strength of 5–8 mT was chosen such that each cluster was actuated below its step-out frequency. The rotation axis of the field was set parallel to the surface (figure 4(A), y-axis). Clusters were recorded while rolling through a workspace of 1.7 mm × 1.3 mm at field frequencies between 0.1 and 10 Hz. The velocity of each cluster was calculated from straight runs ($n = 36$). The maximum perimeter of each cluster in the plane defined by the direction of movement and the vector perpendicular to the rolling surface was measured. This perimeter was estimated by measuring the diameter of the cluster in the direction of movement while the magnetic field was parallel to the surface and while the field was perpendicular to the surface. By assuming a rectangle, the maximum possible perimeter of the cluster was estimated as 2 times the sum of these diameters.

9.4. Localization of IRONSperm clusters using ultrasound images

IRONSperm clusters were injected in a polyethylene vessel with a wall diameter of 1 mm and an inner diameter of 1 mm. This vessel was submerged in water to achieve air-free coupling between the vessel and the ultrasound transducer. A Clarius L15 HD ultrasound transducer was fixed above the vessel, at penetration depth (height) of 5 mm and 65 mm. At a penetration depth of 5 mm, 14 MHz ultrasound waves were used to localize clusters with a diameter of 500 µm. At 65 mm, 10 MHz ultrasound waves were used. The IRONSperm clusters in the vessel were actuated using a rotating permanent magnet from a distance of approximately 5 cm. The magnet had an adhesive force of approximately 3 kg, and rotated at approximately 1 Hz. Ultrasound images at a distance of 5 mm were recorded at 24 fps. Ultrasound images at a distance of 65 mm were recorded at 15 frames per second.

9.5. Drug loading

Drug loading experiments were performed with the anti-cancer drug doxorubicin hydrochloride (DOX-HCl). 10 µl of 1 mM DOX-HCl was mixed with 10 µl IRONSperm solution (2.3×10^5 cells) and 100 µl sterile water. The solution was mixed on a rotary wheel for one hour at room temperature, protecting it from light by covering the vial in aluminum foil. Three replicate samples were prepared. The IRONSperm concentration was determined by cell counting in a Neubauer chamber and calculated using a stock concentration of 2.3×10^7 cells ml^{-1}. Subsequently, one ml of water was added to the sample and centrifuged at 3000 rpm for 5 min to separate the supernatant from the IRONSperm. The supernatant was then measured in a SPARK plate reader, along with a standard row of DOX-HCl (0–10 µM) and reference solutions, that did not contain any IRONSperm. The fluorescence intensity was measured in 96 well plates by applying a 480 nm excitation and 590 nm emission.

The aspect ratios R of the clusters were obtained by measuring the longest and shortest diameter of the clusters in images obtained from bright-field microscopy. Tracing the circumference of the clusters in the

images gave the cluster area. The number of cells in each cluster of 88 clusters was counted manually in the fluorescent images. A folded log-normal distribution was fitted to the aspect ratio distribution of the clusters.

Time-lapse imaging of IRONSperm clusters was used to determine the release of the drugs from IRONSperm over time. Z-Stacks of differential interference contrast and fluorescence channel of the IRONSperm clusters were performed every 30 min over a whole duration of 18 h in aqueous solution. From the total fluorescence intensity per time point, the drug retention inside the cluster was estimated.

9.6. Cytotoxicity

Cytotoxicity tests were performed by seeding cervical carcinoma cells HeLa into 3.5 cm petri dishes (ibidi) at cell density of 50×10^3 cells ml^{-1} in 3 ml complete DMEM high glucose medium with 2 mM L-glutamine, sodium pyruvate, and 10% fetal bovine serum. Then, 200 µl of IRONSperm cluster suspension (3×10^7 sperm cells ml^{-1}) (drug-loaded or plain) was added to each of the samples, with the exception of the control sample. HeLa cells were cultured for 42 h at 37 °C with 5% carbon dioxide. After 42 h, the medium was carefully removed and 1 ml of the staining solution containing 15 µl ethidium homodimer and 2 µl calcein/10 ml medium were added to each sample. Ethidium homodimer stains dead cells red and calcein stains live cells green. Fluorescent microscopy was performed on a Thunder Leica microscope with the standard 510 nm and 475 nm channels for red and green fluorophores, respectively.

Data availability statement

The data that support the findings of this study are available upon reasonable request from the authors.

Acknowledgments

We thank J Simmchen from the Technical University of Dresden for the fabrication of the IRONSperm samples. We thank S Mohanty and M M M Farag from the University of Twente for their help and advice regarding the experimental setup for the actuation and ultrasound imaging experiments. V M thanks Samuel Sanchez for providing laboratory space and resources to perform drug loading and imaging experiments.

Conflict of interest

The authors declare no conflict of interest.

Author contributions

K I N A M developed the theoretical model, designed and performed the actuation and ultrasound experiments, analyzed the data, and wrote the manuscript. V M conceived and designed the microrobots, designed and performed the microscopic imaging and drug loading experiments, and participated in writing and editing the manuscript. L A supervised the work of K I N A M, participated in the design of the actuation and ultrasound experiments, participated in drafting the paper, revised and edited the manuscript. I S M K supervised the work of K I N A M, conceived and designed the microrobots, participated in the design of the actuation and ultrasound experiments and revised and edited the manuscript.

ORCID iDs

Leon Abelmann https://orcid.org/0000-0002-9733-1230
Islam S M Khalil https://orcid.org/0000-0003-0617-088X

References

[1] Jeon S *et al* 2019 Magnetically actuated microrobots as a platform for stem cell transplantation *Sci. Robot.* **4** eaav4317
[2] Sitti M, Ceylan H, Hu W, Giltinan J, Turan M, Yim S and Diller E 2015 Biomedical applications of untethered mobile milli/microrobots *Proc. IEEE* **103** 205–24
[3] Nelson B J, Kaliakatsos I K and Abbott J J 2010 Microrobots for minimally invasive medicine *Annu. Rev. Biomed. Eng.* **12** 55–85
[4] Alapan Y, Yasa O, Yigit B, Yasa I C, Erkoc P and Sitti M 2019 Microrobotics and microorganisms: biohybrid autonomous cellular robots *Annu. Rev. Control Robot. Auton. Syst.* **2** 205–30
[5] Yang Z and Zhang L 2020 Magnetic actuation systems for miniature robots: a review *Adv. Intell. Syst.* **2** 2000082
[6] Sitti M and Wiersma D S 2020 Pros and cons: magnetic versus optical microrobots *Adv. Mater.* **32** 1906766
[7] Xu T, Yu J, Yan X, Choi H and Zhang L 2015 Magnetic actuation based motion control for microrobots: an overview *Micromachines* **6** 1346–64
[8] Palagi S *et al* 2016 Structured light enables biomimetic swimming and versatile locomotion of photoresponsive soft microrobots *Nat. Mater.* **15** 647–53
[9] Zeng H, Wani O M, Wasylczyk P and Priimagi A 2018 Light-driven, caterpillar-inspired miniature inching robot *Macromol. Rapid Commun.* **39** 1700224
[10] Wang W, Castro L A, Hoyos M and Mallouk T E 2012 Autonomous motion of metallic microrods propelled by ultrasound *ACS Nano* **6** 6122–32
[11] Xu T, Xu Li P and Zhang X 2017 Ultrasound propulsion of micro-/nanomotors *Appl. Mater. Today* **9** 493–503
[12] Ismagilov R F, Schwartz A, Bowden N and Whitesides G M 2002 Autonomous movement and self-assembly *Angew. Chem., Int. Ed. Engl.* **41** 652–4
[13] Guix M, Mayorga-Martinez C C and Merkoçi A 2014 Nano/micromotors in (bio)chemical science applications *Chem. Rev.* **114** 6285–322
[14] Wang W, Duan W, Zhang Z, Sun M, Sen A and Mallouk T E 2015 A tale of two forces: simultaneous chemical and

acoustic propulsion of bimetallic micromotors *Chem. Commun.* **51** 1020–3
[15] Alshafeei M E, Hosney A, Klingner A, Misra S and Khalil I S M 2014 Magnetic-based motion control of a helical robot using two synchronized rotating dipole fields *Proc. IEEE RAS and EMBS Int. Conf. on Biomedical Robotics and Biomechatronics* (IEEE Computer Society) pp 151–6
[16] Diller E, Giltinan J, Lum G Z, Ye Z and Sitti M 2016 Six-degree-of-freedom magnetic actuation for wireless microrobotics *Int. J. Robot. Res.* **35** 114–28
[17] Khalil I S M *et al* 2018 Mechanical rubbing of blood clots using helical robots under ultrasound guidance *IEEE Robot. Autom. Lett.* **3** 1112–9
[18] Mahoney A W, Cowan D L, Miller K M and Abbott J J 2012 Control of untethered magnetically actuated tools using a rotating permanent magnet in any position *IEEE Int. Conf. on Robotics and Automation* (Institute of Electrical and Electronics Engineers Inc.) pp 3375–80
[19] Rahmer J, Stehning C and Gleich B 2017 Spatially selective remote magnetic actuation of identical helical micromachines *Sci. Robot.* **2** eaal2845
[20] Ryan P and Diller E 2016 Five-degree-of-freedom magnetic control of micro-robots using rotating permanent magnets *2016 IEEE Int. Conf. on Robotics and Automation* (Institute of Electrical and Electronics Engineers Inc.) pp 1731–6
[21] Xu T, Hwang G, Andreff N and Régnier S 2015 Planar path following of 3-D steering scaled-up helical microswimmers *IEEE Trans. Robot.* **31** 117–27
[22] Yang L and Zhang L 2021 Motion control in magnetic microrobotics: from individual and multiple robots to swarms *Annu. Rev. Control Robot. Auton. Syst.* **4** 509–34
[23] Vilela D, Cossío U, Parmar J, Martínez-Villacorta A M, Gómez-Vallejo V, Llop J and Sánchez S 2018 Medical imaging for the tracking of micromotors *ACS Nano* **12** 1220–7
[24] Aziz A, Pane S, Iacovacci V, Koukourakis N, Czarske J, Menciassi A, Medina-Sánchez M and Schmidt O G 2020 Medical imaging of microrobots: toward *in vivo* applications *ACS Nano* **14** 10865–93
[25] Wang Q and Zhang L 2021 External power-driven microrobotic swarm: from fundamental understanding to imaging-guided delivery *ACS Nano* **15** 149–74
[26] Li L, Wu Z, Yang Y, Hu P, Gao W and Wang L V 2020 Photoacoustic computed tomography guided microrobots for targeted navigation in intestines *in vivo Proc. SPIE* **11240** 112402R
[27] Hortelao A C *et al* 2021 Swarming behavior and *in vivo* monitoring of enzymatic nanomotors within the bladder *Sci. Robot.* **6** eabd2823
[28] Martel S and Mohammadi M 2010 Using a swarm of self-propelled natural microrobots in the form of flagellated bacteria to perform complex micro-assembly tasks *IEEE Int. Conf. on Robotics and Automation* pp 500–5
[29] Aziz A, Medina-Sánchez M, Claussen J and Schmidt O G 2019 Real-time optoacoustic tracking of single moving micro-objects in deep phantom and *ex vivo* tissues *Nano Lett.* **19** 6612–20
[30] Pane S, Iacovacci V, Sinibaldi E and Menciassi A 2021 Real-time imaging and tracking of microrobots in tissues using ultrasound phase analysis *Appl. Phys. Lett.* **118** 014102
[31] Sánchez A, Magdanz V, Schmidt O G and Misra S 2014 Magnetic control of self-propelled microjets under ultrasound image guidance *Proc. IEEE RAS and EMBS Int. Conf. on Biomedical Robotics and Biomechatronics* (IEEE Computer Society) pp 169–74
[32] Wang Q, Du X, Jin D and Zhang L 2022 Real-time ultrasound Doppler tracking and autonomous navigation of a miniature helical robot for accelerating thrombolysis in dynamic blood flow *ACS Nano* **16** 604–16
[33] Aziz A, Holthof J, Meyer S, Schmidt O G and Medina-Sánchez M 2021 Dual ultrasound and photoacoustic tracking of magnetically driven micromotors: from *in vitro* to *in vivo Adv. Healthcare Mater.* **10** 2101077
[34] Feng Y, Chang X, Liu H, Hu Y, Li T and Li L 2021 Multi-response biocompatible Janus micromotor for ultrasonic imaging contrast enhancement *Appl. Mater. Today* **23** 101026
[35] Li J, De Ávila B E F, Gao W, Zhang L and Wang J 2017 Micro/nanorobots for biomedicine: delivery, surgery, sensing and detoxification *Sci. Robot.* **2** eaam6431
[36] Ricotti L, Trimmer B, Feinberg A W, Raman R, Parker K K, Bashir R, Sitti M, Martel S, Dario P and Menciassi A 2017 Biohybrid actuators for robotics: a review of devices actuated by living cells *Sci. Robot.* **2** eaaq0495
[37] Behkam B and Sitti M 2007 Bacterial flagella-based propulsion and on/off motion control of microscale objects *Appl. Phys. Lett.* **90** 023902
[38] Stanton M M, Simmchen J, Ma X, Miguel-López A and Sánchez S 2016 Biohybrid Janus motors driven by *Escherichia coli Adv. Mater. Interfaces* **3** 1500505
[39] Huang H W, Uslu F E, Katsamba P, Lauga E, Sakar M S and Nelson B J 2019 Adaptive locomotion of artificial microswimmers *Sci. Adv.* **5** eaau1532
[40] Yasa O, Erkoc P, Alapan Y and Sitti M 2018 Microalga-powered microswimmers toward active cargo delivery *Adv. Mater.* **30** 1804130
[41] Williams B J, Anand S V, Rajagopalan J and Saif M T A 2014 A self-propelled biohybrid swimmer at low Reynolds number *Nat. Commun.* **5** 1–8
[42] Singh A V, Ansari M H D, Mahajan M, Srivastava S, Kashyap S, Dwivedi P, Pandit V and Katha U 2020 Sperm cell driven microrobots-emerging opportunities and challenges for biologically inspired robotic design *Micromachines* **11** 448
[43] Magdanz V, Sanchez S and Schmidt O G 2013 Development of a sperm-flagella driven micro-bio-robot *Adv. Mater.* **25** 6581–8
[44] Xu H, Medina-Sánchez M, Magdanz V, Schwarz L, Hebenstreit F and Schmidt O G 2018 Sperm-hybrid micromotor for targeted drug delivery *ACS Nano* **12** 327–37
[45] Magdanz V *et al* 2020 IRONSperm: sperm-templated soft magnetic microrobots *Sci. Adv.* **6** 5855–63
[46] Zeng Y and Liu B 2020 Self-propelling and rolling of a sessile-motile aggregate of the bacterium *Caulobacter crescentus Commun. Biol.* **3** 1–8
[47] Sumpter D J T 2006 The principles of collective animal behaviour *Phil. Trans. R. Soc.* B **361** 5–22
[48] Ozkan-Aydin Y, Goldman D I and Saad Bhamla M 2021 Collective dynamics in entangled worm and robot blobs *Proc. Natl Acad. Sci. USA* **118** e2010542118
[49] Elgeti J, Winkler R G and Gompper G 2015 Physics of microswimmers—single particle motion and collective behavior: a review *Rep. Prog. Phys.* **78** 056601
[50] Yu J, Wang B, Du X, Wang Q and Zhang L 2018 Ultra-extensible ribbon-like magnetic microswarm *Nat. Commun.* **9** 1–9
[51] Yigit B, Alapan Y and Sitti M 2020 Cohesive self-organization of mobile microrobotic swarms *Soft Matter* **16** 1996–2004
[52] Dong X and Sitti M 2020 Controlling two-dimensional collective formation and cooperative behavior of magnetic microrobot swarms *Int. J. Robot. Res.* **39** 617–38
[53] Li Z, Zhang H, Wang D, Gao C, Sun M, Wu Z and He Q 2020 Reconfigurable assembly of active liquid metal colloidal cluster *Angew. Chem.* **132** 20056–60
[54] Huang L, Rogowski L, Kim M J and Becker A T 2017 Path planning and aggregation for a microrobot swarm in vascular networks using a global input *2017 IEEE Int. Conf. on Intelligent Robots and Systems* (Institute of Electrical and Electronics Engineers Inc.) pp 414–20
[55] Cappelleri D, Efthymiou D, Goswami A, Vitoroulis N and Zavlanos M 2014 Towards mobile microrobot swarms for additive micromanufacturing *Int. J. Adv. Robot. Syst.* **11** 150
[56] Yigit B, Alapan Y and Sitti M 2019 Programmable collective behavior in dynamically self-assembled mobile microrobotic swarms *Adv. Sci.* **6** 1801837

[57] Yu J, Jin D, Chan K F, Wang Q, Yuan K and Zhang L 2019 Active generation and magnetic actuation of microrobotic swarms in bio-fluids *Nat. Commun.* **10** 1–12
[58] De Lanauze D, Felfoul O, Turcot J P, Mohammadi M and Martel S 2014 Three-dimensional remote aggregation and steering of magnetotactic bacteria microrobots for drug delivery applications *Int. J. Robot. Res.* **33** 359–74
[59] Magdanz V, Vivaldi J, Mohanty S, Klingner A, Vendittelli M, Simmchen J, Misra S and Khalil I S M 2021 Impact of segmented magnetization on the flagellar propulsion of sperm-templated microrobots *Adv. Sci.* **8** 2004037
[60] Magdanz V, Gebauer J, Sharan P, Eltoukhy S, Voigt D and Simmchen J 2019 Sperm–particle interactions and their prospects for charge mapping *Adv. Biosyst.* **3** 1900061
[61] Yung K W, Landecker B and Villani D D 1998 An analytic solution for the force between two magnetic dipoles *Magn. Electr. Sep.* **9** 39–52
[62] Valberg P A and Butler J P 1987 Magnetic particle motions within living cells. Physical theory and techniques *Biophys. J.* **52** 537–50
[63] Jorge G A, Llera M and Bekeris V 2017 Magnetic particles guided by ellipsoidal AC magnetic fields in a shallow viscous fluid: controlling trajectories and chain lengths *J. Magn. Magn. Mater.* **444** 467–71
[64] McNaughton B H, Kehbein K A, Anker J N and Kopelman R 2006 Sudden breakdown in linear response of a rotationally driven magnetic microparticle and application to physical and chemical microsensing *J. Phys. Chem.* B **110** 18958–64
[65] Mahoney A W, Nelson N D, Peyer K E, Nelson B J and Abbott J J 2014 Behavior of rotating magnetic microrobots above the step-out frequency with application to control of multi-microrobot systems *Appl. Phys. Lett.* **104** 144101
[66] Abbott J J, Ergeneman O, Kummer M P, Hirt A M and Nelson B J 2007 Modeling magnetic torque and force for controlled manipulation of soft-magnetic bodies *IEEE Trans. Robot.* **23** 1247–52
[67] Perrin F 1934 Mouvement brownien d'un ellipsoide—I. Dispersion diélectrique pour des molécules ellipsoidales *J. Phys. Radium* **5** 497–511
[68] Box F, Singh K and Mullin T 2018 The interaction between rotationally oscillating spheres and solid boundaries in a Stokes flow *J. Fluid Mech.* **849** 834–59
[69] Liu Q and Prosperetti A 2010 Wall effects on a rotating sphere *J. Fluid Mech.* **657** 1–21
[70] Goldman A J, Cox R G and Brenner H 1967 Slow viscous motion of a sphere parallel to a plane wall—I. Motion through a quiescent fluid *Chem. Eng. Sci.* **22** 637–51
[71] Saffman P G 1965 The lift on a small sphere in a slow shear flow *J. Fluid Mech.* **22** 385–400
[72] Ng A and Swanevelder J 2011 Resolution in ultrasound imaging *Contin. Educ. Anaesth. Crit. Care Pain* **11** 186–92
[73] Wang Q, Yang L, Yu J, Vong C I, Chiu P W Y and Zhang L 2018 Magnetic navigation of a rotating colloidal swarm using ultrasound images *IEEE Int. Conf. on Intelligent Robots and Systems* (Institute of Electrical and Electronics Engineers Inc.) pp 5380–5
[74] Tierno P, Claret J, Sagués F and Cābers A 2009 Overdamped dynamics of paramagnetic ellipsoids in a precessing magnetic field *Phys. Rev.* E **79** 021501
[75] Martel S, Mohammadi M, Felfoul O, Lu Z and Pouponneau P 2009 Flagellated magnetotactic bacteria as controlled MRI-trackable propulsion and steering systems for medical nanorobots operating in the human microvasculature *Int. J. Robot. Res.* **28** 571–82
[76] Fritze A, Hens F, Kimpfler A, Schubert R and Peschka-Süss R 2006 Remote loading of doxorubicin into liposomes driven by a transmembrane phosphate gradient *Biochim. Biophys. Acta Biomembr.* **1758** 1633–40
[77] Lentacker I, De Cock I, Deckers R, De Smedt S C and Moonen C T W 2014 Understanding ultrasound induced sonoporation: definitions and underlying mechanisms *Adv. Drug. Deliv. Rev.* **72** 49–64